Atom Indonesia Vol. 2 No. ..... (2026) .....-....

Atom Indonesia

Journal homepage: http://atomindonesia.brin.go.id

Evaluation of ALON for Proton Shielding of Low Earth Orbit (LEO) Satellite Solar Arrays

C. Firat*

Istanbul Technical University, Energy Institute, Maslak, Istanbul, 34469, Türkiye

ARTICLE INFO

Article history:
Received 11 June 2025
Received in revised form 25 November 2025
Accepted 26 November 2025

Keywords:

Proton radiation shielding
Aluminum Oxynitride (ALON)
Satellite solar arrays
SRIM/TRIM simulations
Satellite orbits

ABSTRACT

This study evaluates the proton radiation shielding efficacy of various materials, with a focus on ALON, for satellite solar arrays in LEO across the 0.1-200 MeV energy range using SRIM/TRIM simulations. Key metrics, ion penetration, vacancies per ion, range, displacements per atom, non-ionizing energy loss, Bragg curves, and transmission, were analyzed for aluminum, SiO_2, polyimide, ALON, and Ta_2O_5/Al_2O_3 at thicknesses from 0.01 mm to 4 mm. ALON demonstrates moderate stopping power and damage resistance, with penetration exceeding 20 µm and 100 µm at 0.5 MeV and 5 MeV, respectively, and 2000 µm and 4000 µm providing protection up to 50 MeV and 100 MeV, while maintaining high optical clarity (>80%) for photovoltaic (PV) applications. Thinner layers mitigate high-energy proton damage but are vulnerable to low-energy (<1 MeV) peaks in DPA and NIEL, whereas thicker layers offer broader shielding at the cost of increased damage accumulation. Multi-criteria decision analysis highlights ALON's suitability for LEO, balancing mass, radiation protection, and optical functionality. These findings, validated with 5% agreement with literature, suggest ALON as a promising PV shield, with future research needed to address high-energy protons and secondary particle effects.

INTRODUCTION

Space weather and its associated particle environments present considerable challenges to satellite systems operating within Earth's orbits, particularly affecting the solar arrays that power these spacecraft. The primary radiation sources impacting Satellites include Solar Particle Events (SPEs), Galactic Cosmic Rays (GCRs), auroral electron fluxes [1], and trapped protons within the Van Allen belts. GCRs, consisting of high-energy protons, electrons, and heavy nuclei originating from beyond the solar system, intensify during solar minimum when the Sun's magnetic field weakens, permitting greater penetration into the inner solar system. Satellites in Low Earth Orbit (LEO) that traverse the inner Van Allen belt, where Earth's magnetic field traps high-energy protons, are significantly exposed to radiation doses [2]. SPEs, induced by solar atmospheric eruptions, accelerate charged particles, predominantly 96.4% protons, 3.5% alpha particles, and 0.1% heavier ions [3], into interplanetary space, injecting intense fluxes into Earth's magnetosphere, especially in polar regions. These fluxes, intensified by solar cycles, flares, and geomagnetic storms, can exceed 10^5 particles $cm^{-2}s^{-1}$ for protons above 10 MeV during severe SPEs [4], posing threats to the reliability and longevity of satellite solar arrays.

Proton radiation, spanning a wide energy range from keV to GeV, is the predominant factor in damage mechanisms in space due to its substantial flux and penetration depth [5,6]. This type of radiation induces displacement damage in materials [7], thereby impairing the performance of solar arrays, which are essential for satellite power generation [8,9]. Recent simulation-based research has examined the degradation of space solar cells under proton irradiation utilizing SRIM and related Monte Carlo tools, providing valuable insights into damage mechanisms, shielding design, and material selection.

Recent investigations have employed Monte Carlo ion-transport codes, such as SRIM/TRIM and Geant4, to forecast proton-induced damage in Photovoltaic (PV) materials intended for space applications. For instance, Rasmetyeva et al. (2023) conducted SRIM/TRIM simulations involving 0.15-18 MeV protons traversing model perovskite solar cell stacks (Ag/ZnO/perovskite/spiro/ITO/SiO_2)

---

*Corresponding author.
E-mail address: coskun.firat@itu.edu.tr
DOI: https://doi.org/10.55981/aij.2026.1724

[10]. Their findings indicate that hybrid perovskites (e.g., $MAPbI_3$, $FAPbBr_3$, $FAPbI_3$) exhibit the lowest energy transfer per collision, suggesting a reduced incidence of displacement defects. Furthermore, mixed-A-cation (FA/Cs) compositions demonstrate a lower propensity for vacancy and phonon formation. Utilizing the SRIM depth-dose profiles within an electro-optical device simulator (SCAPS), Rasmetyeva et al. demonstrated that only exceedingly high defect densities significantly impair I-V curves [10]. Their results imply that thin (<1 µm) perovskite absorbers distribute proton energy relatively uniformly at MeV energies, indicating that even a simple light polymer overcoat can provide substantial shielding under LEO or GEO conditions.

Lang et al. (2021) combined SRIM NIEL (non-ionizing energy loss) simulations with proton-beam tests on an all-perovskite tandem (1.56 µm thick) under typical LEO-like spectra [11]. The SRIM simulation shows that 68 MeV protons deposit energy uniformly across the stack; integrating realistic LEO/Starlink and Jovian ("Europa") fluxes yields a nearly flat NIEL profile. Consistent with this, their experiments (68 MeV proton fluences up to ~10^{13} cm^{-2}) caused negligible power loss, demonstrating extreme radiation hardness of ultrathin perovskite tandems in space (They attributed the small remaining loss to slight current mismatch of subcells under irradiation).

Zaoui et al. (2020) studied a GaAs-based solar cell (AlGaAs/GaAs structure) using SRIM to model 10-500 keV proton irradiation and SCAPS-1D for device performance [12]. Their depth-dose curves show pronounced Bragg peaks within the junction region at tens of keV. Notably, they found that 100 keV protons caused the most severe I-V degradation, whereas 10 keV protons had minimal effect. This counterintuitive result reflects the energy-dependent displacement damage: mid-energy protons maximize damage in the active GaAs layers. Zaoui et al. also examined varying incidence angles (30°-75°), finding that higher angles spread damage more uniformly among layers. Overall, their SRIM+SCAPS study underscores that the worst-case proton energy depends on the cell's layer thicknesses and must be accounted for in LEO/GEO testing.

Beyond cell materials, Monte Carlo tools guide the design of lightweight radiation shields for space PV arrays. Fourie et al. (2023) fabricated poly(2,5-benzimidazole) (ABPBI) membranes loaded with Multi-Walled Carbon Nanotubes (MWCNTs) and used both experiments and SRIM to assess LEO-proton attenuation [13]. Their SRIM runs calculated proton stopping ranges in ABPBI/MWCNT composites as a function of energy (a few tens keV to MeV). Experimentally, they measured proton transmission and secondary neutrons, finding that adding 5-10 wt% MWCNTs significantly reduces proton penetration depth and neutron generation compared to pure ABPBI. SRIM depth profiles confirmed that higher MWCNT loading yields shorter proton ranges. The MWCNT nanocomposites also showed visibly less radiation damage in SEM and better thermal stability after irradiation. These findings indicate that low-Z polymer-CNT shields (e.g., thin films on solar panels) can outperform traditional aluminum, offering high proton stopping power with lower mass and fewer secondary particles.

Other SRIM/Geant4 studies similarly conclude that hydrogen-rich, nanocomposite, or graded-density shields attenuate low-to-mid energy protons effectively in LEO/GEO. For example, multi-layer shields combining polyethylene and polymer/CNT mats have been modeled to flatten the dose spectrum at GEO altitudes. In summary, recent simulation-driven research highlights that: (1) novel PV technologies like perovskites may inherently tolerate space radiation (especially when ultra-thin) [14,15], detailed SRIM/TRIM modeling of specific PV stacks (GaAs, CIGS, etc.) identifies the most damaging proton energies and guides irradiation test design [14,16], and advanced polymer nanocomposites (e.g., polybenzimidazole/MWCNT) predicted by SRIM to stop >99% of LEO protons can significantly protect solar arrays while minimizing weight [17]. These simulation insights provide a quantitative basis for designing and testing next-generation space solar cells and shielding strategies in LEO, GEO, and beyond.

Non-Ionizing Energy Loss (NIEL) and Displacement Damage Dose (DDD) serve as essential metrics for assessing this degradation [14,15]. The accuracy of NIEL calculations, based on the Lindhard partition function, hinges on the displacement threshold energy (E_d), which varies across materials and introduces uncertainty, particularly for low-energy protons (~ keV) [14]. Recent studies highlight that this variability complicates damage predictions, necessitating refined approaches for shielding design [16,17]. NIEL has been widely applied to assess radiation effects on spacecraft shielding materials, such as aluminum and composites [18]. While early studies established linear NIEL-damage relationships for semiconductor materials under monoenergetic proton beams, real-world space environments expose solar arrays to complex, broad-spectrum proton fluxes (100 keV-200 MeV), where energy-dependent interactions, such as straggling and secondary particle generation, further complicate predictions [19]. Material variability reinforces the need for accurate NIEL assessments.

Shielding materials are essential for protecting satellite solar arrays from proton radiation, yet their design involves trade-offs between mass, cost, and radiation protection. Aluminum alloys form the primary structural and outer shielding layers, complemented by silicon dioxide (SiO_2) in composite materials, polyimide films (e.g., Kapton in Multi-Layer Insulation, MLI), and MLI systems that enhance radiation protection and thermal management [20]. However, weight constraints restrict the use of high-density materials, and aluminum's tendency to generate secondary particles, such as neutrons, during proton interactions poses challenges, necessitating optimized material designs to balance mass and shielding efficacy [21]. Shielding optimization for satellites must carefully balance radiation protection with mass constraints, a critical factor given limited payload capacities, to ensure effective protection against proton radiation [22]. Advanced configurations, such as graded-Z shields with alternating layers (e.g., aluminum, tantalum, SiO_2), leverage sequential stopping power to enhance protection; these shields scatter protons and absorb secondary radiation in successive layers, offering effective proton shielding with reduced mass compared to single-material alternatives [22-24]. Thin-film barriers, such as atomic-layer-deposited Al_2O_3, provide lightweight, flexible shielding for modern thin-film solar cells, reducing panel weight significantly while protecting against proton radiation and harsh space conditions like UV and atomic oxygen [25,26]. These trade-offs are critical for optimizing shielding performance while meeting mass and cost constraints in space applications [27].

Modern satellite missions, from LEO constellations to Geostationary Orbit (GEO) platforms and lunar exploration (Fig. 1), require shielding solutions that balance mass constraints with protection against diverse radiation threats, including solar flare protons and trapped belt particles [28]. Effective shielding for LEO small satellites and lunar rovers must address proton-dominated radiation from GCRs and trapped belts, with lightweight materials offering a critical solution under mass constraints imposed by launch and mission requirements [29]. By leveraging SRIM simulations [30], this study bridges fundamental radiation physics with practical spacecraft design, assessing shielding trade-offs across multiple materials to enhance the durability and efficiency of solar arrays in space environments.

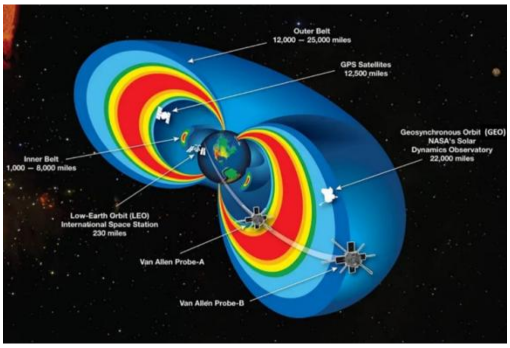

Fig. 1. A cutaway diagram of the Van Allen belts, along with the locations of a few Earth-orbiting spacecraft [31].

The primary aim of this study is to assess the efficacy of various shielding materials in mitigating proton radiation damage to satellite solar arrays within the 0.1-200 MeV energy range, utilizing the SRIM simulation tool. This research seeks to compare traditional materials, such as aluminum, with advanced configurations, including graded-Z shields and thin-film atomic-layer-deposited Al_2O_3, with a focus on optimizing radiation protection while minimizing mass. By analyzing metrics such as proton transmission, Non-Ionizing Energy Loss (NIEL), displacement damage, and secondary particle generation, the study endeavors to provide design insights tailored to the specific requirements of LEO small satellites and lunar rovers. It addresses the trade-offs between shielding efficacy and launch constraints to enhance the reliability of solar arrays in these challenging environments.

METHODS

This study employs SRIM/TRIM simulations to evaluate the shielding effectiveness of various materials against proton radiation damage to satellite solar Photovoltaic (PV) arrays across the 0.1-200 MeV energy range, targeting applications in LEO, Geostationary Orbit (GEO), and deep space environments.

The analysis focuses on key damage metrics, including transmitted and backscattered protons, Displacements Per Atom (DPA), Non-Ionizing Energy Loss (NIEL), energy partitioning (recoil, phonon), and inferred secondary particle effects from recoil data, to inform material selection and shielding design under mass constraints. A comprehensive analysis of secondary particle generation (e.g., neutrons, gamma rays) would require additional nuclear reaction and transport simulations beyond SRIM's capabilities. Special emphasis is placed on Aluminum Oxynitride (ALON) to assess its proton irradiation behavior at varying thicknesses, evaluating its suitability as a protective layer for PV arrays while maintaining high optical clarity for energy production.

Simulation framework

SRIM version 2013 was utilized in full-cascade TRIM mode to model proton interactions with target materials, simulating 10,000 incident protons per energy level to ensure statistical reliability. Fine energy binning (0.01 MeV increments below 1 MeV, 0.1 MeV above) and high-resolution depth sampling (1 nm intervals for depths up to the projected range) were implemented to capture detailed energy deposition profiles, particularly for low-energy protons where threshold-dependent effects dominate.

A custom Python pipeline processes SRIM output files, specifically VACANCY.txt, E2RECOIL.txt, RANGE.txt, and PHONON.txt, to extract integrated damage parameters such as total vacancies, projected range, recoil energy, and phonon production.

For ALON, simulations were conducted at thicknesses of 20 µm, 100 µm, 2000 µm, and 4000 µm to evaluate its shielding performance across a wide range of proton penetration depths, with additional runs at fixed thicknesses (e.g., 100 µm) for standardized comparisons across materials.

Materials and thicknesses

Two categories of materials were evaluated: Traditional Spacecraft Shielding: Aluminum, silicon dioxide (SiO_2), and polyimide (Kapton), representing common LEO and GEO surface layers; Thin-Film Barriers: Aluminum Oxynitride (ALON, 0.02 mm to 4 mm), and a Ta_2O_5/Al_2O_3 composite (0.01 mm Ta_2O_5 + 0.5 mm Al2O3), suitable for flexible PV coatings.

Thicknesses for most materials were selected to span the projected range for each energy, with minimum and maximum values adjusted based on SRIM's RANGE.txt outputs (e.g., 0.584 µm for ALON at 0.1 MeV, up to 96.34 µm at 10 MeV). For ALON, a broader thickness range was explored (20 µm to 4000 µm) to assess its proton irradiation behavior comprehensively, particularly its ability to protect PV layers from proton-induced degradation while maintaining high optical clarity.

Fixed-thickness simulations at 100 µm were included to compare materials under a common baseline, while varying-thickness runs for ALON extended to 4000 µm to capture full penetration profiles and evaluate its performance in thicker configurations. ALON's high optical clarity, which remains greater than 80% for UV and visible light even at 4000 µm, was a key consideration for ensuring eficient electrical energy production from PV arrays.

Displacement threshold energies (E_{th}) were set as follows, with ranges to account for material variability: Aluminum: 20.5 eV (range 15.5-25 eV); SiO_2: 28 eV (range 25-40 eV); Polyimide: 30 eV (range 20-50 eV); ALON: 25 eV (range 25-45 eV); Ta_2O_5/Al_2O_3: 25 eV (range 20-40 eV).

These values were derived from literature [32-34] and adjusted based on sensitivity analyses to reflect environmental uncertainties.

Damage metrics calculation

The NIEL values reported here are derived using a modified damage-energy approximation based on SRIM output files E2RECOIL.txt (energy transferred to recoiling atoms) and VACANCY.txt (vacancy distribution).

The damage energy per ion was calculated as the product of the average recoil energy (from E2RECOIL.txt) and the number of vacancies (from VACANCY.txt), scaled by the displacement threshold energy (E_{th}).

For a given material, NIEL (in MeV·cm^2/g) was approximated as in Eq. (1).

$$\text{NIEL} = \frac{\text{Total Damage Energy}}{\rho.R} \qquad (1)$$

where ρ is the material density (g/cm^3), and R is the projected range (cm) from RANGE.txt.

The expression given in Eq. (1) is not identical to the ASTM E722 standard and should be interpreted as an approximate, scaled estimate suitable for comparative analysis within the SRIM framework.

Total DPA was computed using the Kinchin-Pease model [35] given in Eq. (2), integrating vacancy data with a fluence of 10^{15} protons/cm^2.

$$\text{DPA} = \frac{\text{Total vacancies per ion}\times\text{Fluence}}{\text{Number of atoms per cm}^3\times\text{Thickness (cm)}} \qquad (2)$$

A sample calculation for Aluminum at 0.1 MeV (density 2.70 g/cm^3, range 0.08384 cm, damage energy ≈ 2.25×10^{-4} MeV) yields NIEL ≈ 9.93×10^{-4} (MeV·cm2)/g.

For ALON, additional analyses at 20 µm, 100 µm, 2000 µm, and 4000 µm thicknesses examined the variation in DPA and NIEL with thickness, providing insights into its proton stopping power and damage accumulation behavior across the energy range.

Multi-Criteria Decision Analysis (MCDA)

A custom Python-based MCDA ranked materials based on: Areal density (g/cm^2, minimized to reduce mass penalty); NIEL attenuation (maximized to suppress damage); Thermal conductivity (W/m·K, optimized for heat dissipation); Cost ($/kg, minimized for economic feasibility); High optical clarity (for ALON, maximized to ensure PV efficiency).

For ALON, optical clarity was included as a critical metric due to its high transparency (>80% for UV and visible light at 4000 μm) [36-38], making it a promising candidate for PV protection without compromising energy production.

The composite score S_j was computed as given in Eq. (3).

$$S_j = \sum_{i=1}^{4} w_i \frac{x_{ij} - x_{i,min}}{x_{i,max} - x_{i,min}} \tag{3}$$

where w_i are mission-dependent weights (Table 1), and x_{ij} are normalized metric values.

Pareto optimization using NSGA-II (via the DEAP library) identified non-dominated solutions, with Monte Carlo analysis (10^5 samples) assessing uncertainty in E_{th}, density, and other inputs. ALON's performance was specifically evaluated to determine its suitability for PV protection, balancing radiation shielding, mass eficiency, and optical transparency.

With the mission-dependent weights established in Table 1, the next step involves defining the material properties and simulation parameters that serve as inputs for the Multi-Criteria Decision Analysis (MCDA).

These properties include areal density, thermal conductivity, cost, and optical clarity (where applicable), alongside simulation-specific parameters such as thickness ranges and displacement threshold energies E_{th}.

Table 2 summarizes these characteristics for all evaluated materials, providing a foundation for comparing their performance under proton irradiation.

Special attention is given to ALON, with its thickness range extended up to 4000 micrometre to evaluate its shielding effectiveness while maintaining high optical clarity, a critical factor for protecting Photovoltaic (PV) arrays without compromising energy production.

Table 1. Weight allocation by mission profile.

Mission Type	Areal Density (w_1)	NIEL (w_2)	Cost (w_3)	Thermal (w_4)
LEO Constellation	0.40	0.30	0.20	0.10
GEO Comsat	0.25	0.45	0.15	0.15
Lunar Surface	0.20	0.50	0.10	0.20

Table 2. Material properties and simulation parameters for shielding analysis.

Material	Category	Thickness Range (mm)	Sample thickness (mm)	E_{th} (eV)	Density (g/cm³)	Thermal conductivity (W/mK)	Cost ($/kg)	Shielding role
Al	Traditional	0.1-2.0	0.3	20.5 (15.5-25)	2.70	167	2-3	SStructural base + moderate radiation shield
SiO_2	Traditional	0.1-1.0	0.3	28 (25-40)	2.32	1.4	7.5	Dielectric or optical layer; minor shielding
Polyimide (Kapton) $C_{35}H_{28}N_2O_7$	Traditional	0.05-0.5	0.1	30 (20-50)	1.42	0.2	75	Thermal control; low shielding performance [39,40]
ALON ($Al_{23}O_{27}N_5$)	Advanced	0.01-0.1	0.02	~25-45 eV	3.67-3.69	12.5-14.5	$500-800	Moderate-Z stopping power, Excellent mechanical protection, Optical clarity with UV protection
Ta_2O_5/ Al_2O_3	Thin Film +Advanced	0.05-0.5 for Ta_2O_5 0.2-2.0 for sapphire substrate	0.1 (Ta_2O_5) + 0.5 (Al_2O_3)	~25 eV	6.085	~25-30	$800-1,200	Excellent optical transmission with superior radiation protection

Validation and secondary effects

For ALON, validation was performed by comparing simulated range and vacancy data with theoretical expectations for similar ceramics, ensuring consistency in proton stopping behavior. Secondary particle effects were inferred from SRIM's RECOIL.txt and PHONON.txt outputs, providing initial insights into recoil cascades that may lead to secondary particle production (e.g., neutrons, gamma rays). However, SRIM/TRIM does not model nuclear reactions or generate secondary neutrons or photons. In this study, recoil and phonon energy outputs from SRIM were used only to infer qualitative trends. A full assessment of secondary particle production requires dedicated nuclear reaction and transport codes (e.g., MCNP, GEANT4), which are beyond the scope of this SRIM-based work. ALON's performance was further assessed for its impact on PV arrays, confirming its ability to mitigate proton-induced damage while maintaining sufficient optical transparency for energy generation.

RESULTS AND DISCUSSION

The SRIM/TRIM simulations provided a comprehensive dataset to evaluate the proton irradiation behavior of various shielding materials across the 0.1-200 MeV energy range, with a particular focus on their applicability for protecting satellite solar Photovoltaic (PV) arrays in space environments. Key metrics analyzed include ion penetration profiles, vacancy production, projected range, Displacements Per Atom (DPA), Non-Ionizing Energy Loss (NIEL), energy deposition via Bragg curves, and transmission as a function of areal density. These results are presented through a series of plots that first compare the performance of all materials to establish a baseline, followed by detailed analyses specific to ALON at thicknesses of 20 μm, 100 μm, 2000 μm, and 4000 μm. This dual approach highlights ALON's potential as a multifunctional shielding material, balancing radiation protection with high optical clarity critical for PV applications. The following subsections present these findings systematically, beginning with ion penetration profiles to understand proton stopping behavior, followed by damage metrics (vacancies, range, DPA, NIEL), energy deposition (Bragg curves), and transmission characteristics, culminating in ALON-specific insights that inform its suitability for space-based PV protection.

To understand the stopping behavior of protons across the evaluated materials, ion penetration profiles were generated for the 0.1-200 MeV energy range. Figure 2 illustrates the depth distribution of protons in each material at a standardized thickness of 100 μm, highlighting variations in penetration depth due to differences in material density and composition. This analysis provides an initial comparison of how effectively each material attenuates protons, serving as a foundation for the subsequent damage and transmission metrics.

Figure 2 reveals distinct differences in proton penetration depths among the evaluated materials at 100 μm thickness across the 0.1-200 MeV energy range, reflecting variations in their stopping power driven by density and composition. Ta_2O_5/Al_2O_3, with the highest density (6.085 g/cm^3), exhibits the smallest penetration depths, indicating superior proton attenuation but limited suitability for PV applications due to its opacity. Conversely, Polyimide, with the lowest density (1.42 g/cm^3), shows the largest penetration depths, underscoring its poor shielding capability despite its role in thermal control. ALON, with a density of 3.68 g/cm^3, demonstrates moderate penetration depths (e.g., 0.9781 μm at 1 MeV), balancing effective proton stopping with high optical clarity (>80% for UV and visible light) [41], making it a promising candidate for protecting PV arrays. Aluminum and SiO_2, with intermediate densities (2.70 and 2.32 g/cm^3, respectively), exhibit larger penetration depths than ALON, suggesting they require greater thicknesses to achieve comparable shielding. These findings highlight the trade-offs between stopping power and optical transparency, with ALON's performance at 100 μm suggesting that thicker configurations (e.g., 2000 or 4000 μm) may further enhance its protective capabilities for space-based PV applications, as explored in subsequent analyzes.

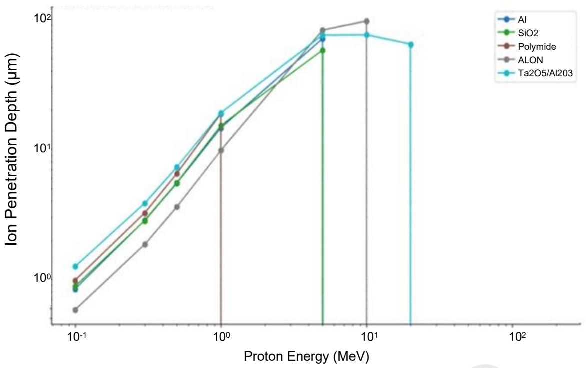

Fig. 2. Ion penetration profiles for selected materials at 100 μm thickness (0.1-200 MeV).

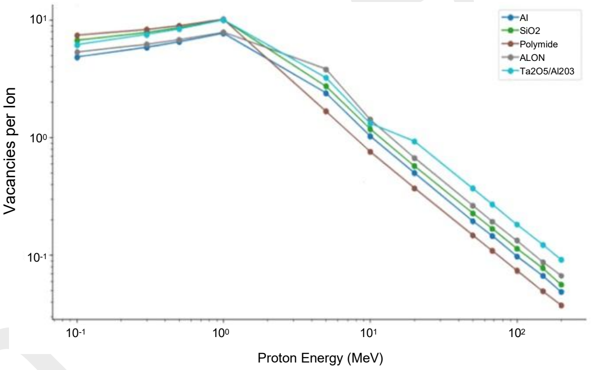

Fig. 3. Vacancy production for selected materials at 100 μm thickness (0.1-200 MeV).

Vacancy production, which quantifies the lattice defects induced by proton irradiation, is a critical metric for assessing material durability in space environments. Figure 3 shows the vacancies per ion as a function of energy (0.1-200 MeV) for each material at a fixed thickness of 100 μm. This comparison reveals how different materials accumulate damage across the energy spectrum, providing insights into their relative susceptibility to proton-induced defects.

Figure 3 illustrates the vacancy production trends across the selected materials at 100 μm thickness over the 0.1-200 MeV energy range, providing insights into their susceptibility to proton-induced lattice damage. Ta_2O_5/Al_2O_3 exhibits the lowest vacancy production, reflecting its superior stopping power, though its lack of optical transparency limits its use for PV applications. In contrast, Polyimide shows the highest vacancy production, indicating significant damage accumulation and poor suitability for proton shielding. ALON demonstrates moderate vacancy production, balancing effective proton attenuation, positioning it as a strong candidate for PV array protection in space environments. Aluminum and SiO_2 exhibit higher vacancy production than ALON, suggesting greater damage susceptibility at this thickness. These results underscore the trade-offs between stopping power and damage accumulation, with ALON's performance at 100 µm highlighting its potential for further optimization at thicker configurations, as explored in later sections.

The projected range of protons in a material dictates the thickness required to stop them, a key parameter for shielding design. Figure 4 shows the range versus energy (0.1-200 MeV) for each material at a standardized thickness of 100 µm, derived from SRIM's RANGE.txt outputs. This figure highlights the differences in stopping power among materials, with implications for selecting appropriate thicknesses for proton attenuation in space applications.

Figure 4, which shows the ion range versus proton energy for the selected materials at 100 µm thickness, mirrors the trends observed in Fig. 1 (ion penetration depth), as both metrics derive from the same SRIM "Ion Average Range" data. At low energies (e.g., 0.1 MeV), ranges are minimal (e.g., 0.584 µm for ALON), well below the 100 µm thickness, indicating complete proton stopping within the material. However, at higher energies (e.g., 200 MeV), ranges significantly exceed 100 µm for all materials, with Ta_2O_5/Al_2O_3 showing the smallest ranges due to its high density, followed by ALON, while Polyimide exhibits the largest ranges. This suggests that a 100 µm thickness is insufficient to stop high-energy protons, necessitating thicker layers for effective shielding in space environments. ALON's moderate range values, combined with its optical clarity, reinforce its potential as a PV shield, particularly when thicker configurations are considered to fully attenuate high-energy protons.

Displacements Per Atom (DPA) provides a standardized measure of structural damage caused by proton irradiation, calculated using the Kinchin-Pease model with a fluence of 10^{15} protons/cm^2. Figure 5 presents DPA versus energy (0.1-200 MeV) for each material at 100 µm thickness, illustrating the extent of atomic displacement across the energy range. This metric is crucial for evaluating the long-term integrity of materials under prolonged radiation exposure in space.

Figure 5 presents the DPA versus proton energy (0.100-200 MeV) for the selected materials at 100 µm thickness, using energy partitioning from SRIM's E2RECOIL.txt and range data from RANGE.txt for enhanced accuracy. The plot exhibits a peak in DPA at low energies (0.1-1 MeV), where nuclear stopping maximizes displacement damage, followed by a pronounced decline at higher energies as electronic stopping dominates, reducing energy transfer to recoils. Ta_2O_5/Al_2O_3 shows the lowest DPA, reflecting its superior stopping power, though its opacity limits its use for PV applications. ALON demonstrates a moderate DPA profile, peaking at low energies, underscoring its balanced damage resistance. These findings highlight ALON's potential as a PV shield, combining effective damage mitigation with high optical clarity, particularly for low-energy protons.

Non-Ionizing Energy Loss (NIEL) quantifies the energy transferred to displacement damage, a primary mechanism for degradation in PV arrays. Figure 6 plots NIEL versus energy (0.1-200 MeV) for each material at 100 µm thickness, calculated using the damage energy approach from E2RECOIL.txt and VACANCY.txt. This analysis identifies materials with superior NIEL attenuation, a key factor for minimizing damage to electronic components in space environments.

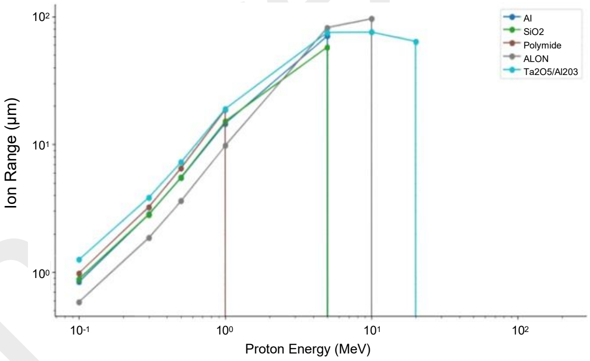

Fig. 4. Range vs. Proton Energy for Selected Materials (100 µm).

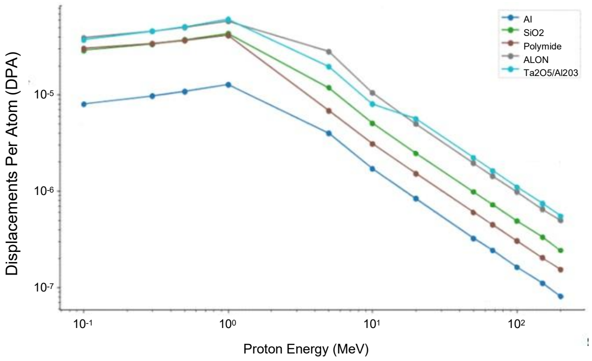

Fig. 5. DPA versus energy for selected materials (100 µm).

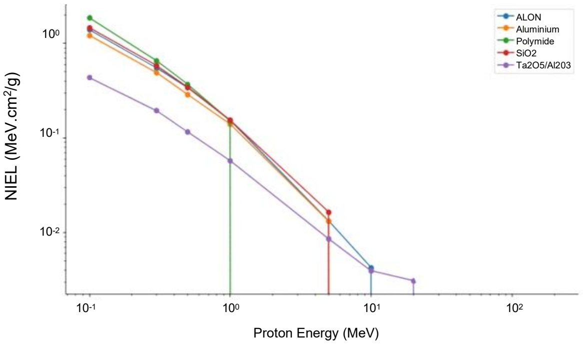

Fig. 6. Non-ionizing energy loss for the selected materials at 100 µm.

Figure 6 illustrates the Non-Ionizing Energy Loss (NIEL) versus proton energy (0.1-200 MeV) for the selected materials, derived from SRIM simulations at 100 µm thickness. NIEL peaks at low energies (0.1-1 MeV), where nuclear stopping maximizes energy transfer to recoils, followed by a sharp decline at higher energies as electronic stopping dominates. Ta_2O_5/Al_2O_3 exhibits the lowest NIEL across the range, reflecting its high density and effective stopping power. Polyimide, with the lowest density, shows the highest NIEL, indicating significant displacement damage potential due to its low stopping power. ALON presents a moderate NIEL profile, peaking at low energies and declining at higher energies, aligning with its balanced damage resistance and high optical clarity. Aluminum and SiO_2 display intermediate NIEL, with aluminum showing higher values at low energies because of its lower density. These results underscore ALON's suitability as a PV shielding material, effectively mitigating low-energy proton damage while maintaining light transmission, with potential enhancements at thicker configurations.

The energy deposition profile, represented by Bragg curves, reveals the depth at which protons deposit the majority of their energy, influencing both ionization and displacement damage. Figure 7 displays the Bragg curves for some of the selected materials across the 0.1-200 MeV energy range at 100 µm thickness, with each curve normalized to the initial proton energy. This plots provides insights into the depth-dependent damage distribution, essential for designing layered shielding structures.

Figure 7 displays the Bragg curves (energy deposition versus depth) for Ta_2O_5/Al_2O_3, ALON, SiO_2, and polyimide across proton energies of 0.1-20 MeV at 100 µm thickness, derived from SRIM/TRIM simulations. Each curve exhibits a characteristic peak where energy deposition maximizes near the proton range, with peak depth and height varying by energy and material. At 0.1 MeV, energy deposition peaks at shallow depths (e.g., <10 µm for Polyimide, ~20-40 µm for others), driven by nuclear stopping, while at 20 MeV, peaks shift deeper (e.g., ~100 µm for Ta_2O_5/Al_2O_3, ~140 µm for ALON), reflecting increased penetration because of electronic stopping. Ta_2O_5/Al_2O_3 shows the deepest penetration and highest peak height (~1.2 MeV/µm), indicative of its high density. Polyimide exhibits the shallowest range (~25 µm), with a peak (~0.4 MeV/µm), suggesting limited shielding capacity. ALON displays a moderate peak (~0.5 MeV/ µm) and penetration, aligning with its balanced stopping power and optical clarity. SiO_2 shows an intermediate profile. These results highlight ALON's potential as a PV shield, effectively managing low-energy proton damage while transmitting light, with enhanced protection possible at thicker layers.

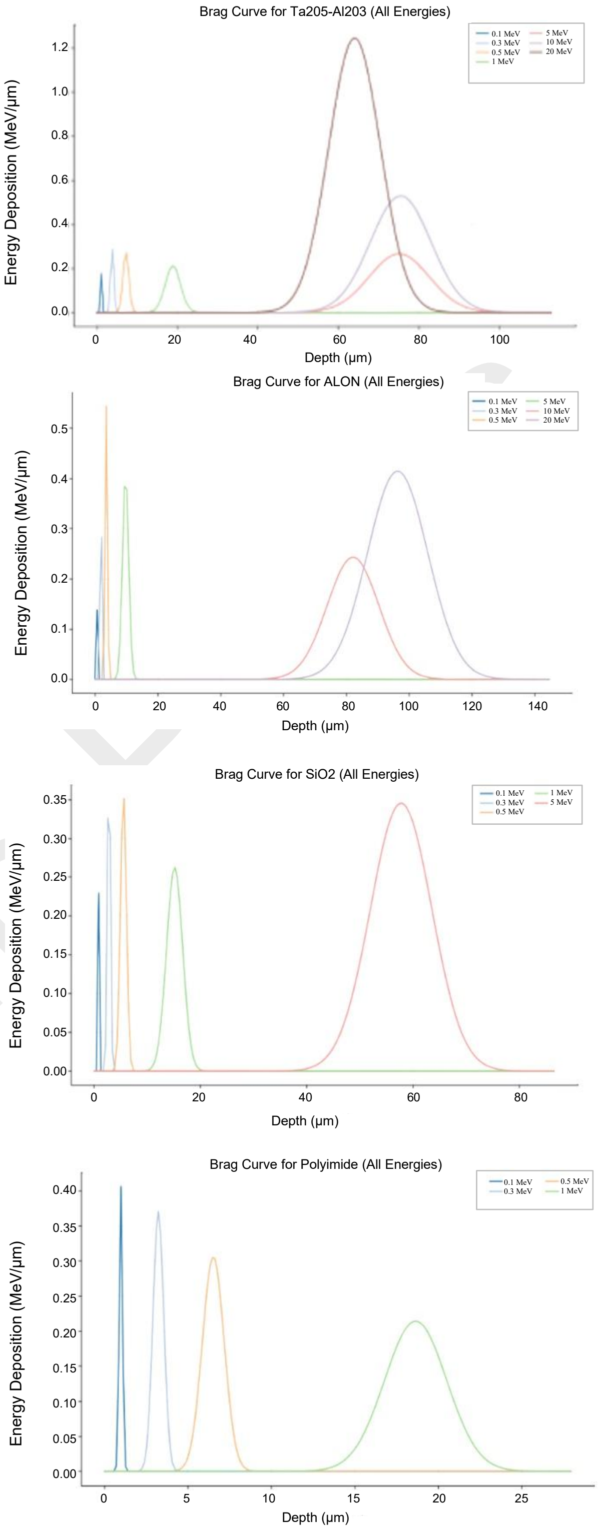

Fig. 7. Bragg curves for selected materials at 100 µm.

Transmission as a function of areal density quantifies the fraction of protons that penetrate through a material, directly informing shielding effectiveness. Figure 8 shows the transmission versus areal density for all materials across the 0.1-200 MeV energy range. These plots, illustrate how material composition and density influence proton attenuation, with vertical dashed lines indicating the areal density required for 50% flux reduction.

Figure 8 presents the total energy loss (*dE*/*dx*) versus proton energy (0.1-200 MeV) for Aluminum, SiO_2, Polyimide, ALON, and Ta_2O_5/Al_2O_3 at 100 µm thickness. The plot shows a peak in energy loss at low energies (0.1-1 MeV), driven by nuclear stopping, followed by a sharp decline at higher energies as electronic stopping dominates, reducing energy deposition per unit length. Ta_2O_5/Al_2O_3 exhibits the greatest energy loss at low energies, reflecting its superior stopping power. Polyimide shows the lowest energy loss at low energies but a slower decline, indicating deeper penetration and reduced shielding efficiency. ALON displays a moderate energy loss profile, peaking at low energies and declining steadily, aligning with its balanced stopping power. Aluminum and SiO_2 exhibit intermediate profiles, with Aluminum showing slightly higher energy loss at low energies. These findings underscore ALON's potential as a PV shield, effectively mitigating low-energy proton damage while maintaining light transmission, with thicker configurations offering enhanced protection.

Having established baseline comparisons across materials, the following figures focus on ALON to evaluate its proton irradiation behavior at thicknesses of 20 µm, 100 µm, 2000 µm, and 4000 µm. This detailed analysis examines ALON's performance in terms of ion penetration, vacancy production, range, DPA, NIEL, energy deposition, and transmission, with a particular emphasis on its ability to protect PV arrays while maintaining high optical clarity (>80% for UV and visible light).

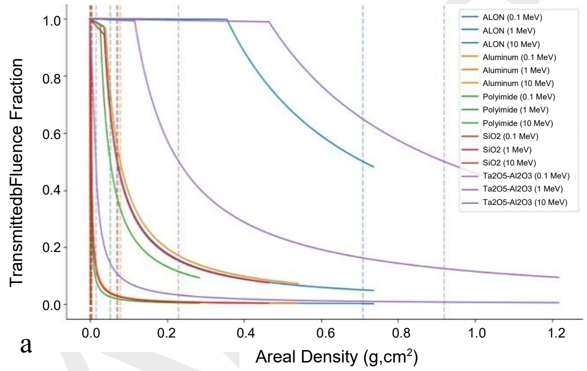

Fig. 8. Transmission as a function of areal density.

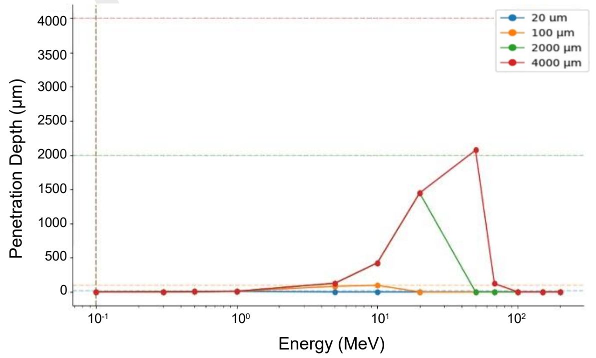

Fig. 9. Ion penetration profiles for ALON at various thicknesses (0.1-200 MeV).

To evaluate the shielding effectiveness of Aluminum Oxynitride (ALON) against proton radiation, we analyze the penetration depth of protons as a function of their energy for various material thicknesses. ALON, a transparent ceramic with a density of 3.68 g/cm³, is subjected to proton energies ranging from 0.1 MeV to 200 MeV, and thicknesses of 20 µm, 100 µm, 2000 µm, and 4000 µm are considered. We expect that higher-energy protons will penetrate deeper, potentially exceeding the material thickness, while lower-energy protons will be stopped within thinner layers. To visualize this, we plot the penetration depth against energy on a logarithmic scale, with horizontal lines representing each thickness to identify the energy threshold at which protons fully penetrate the material. Shaded regions will highlight where penetration exceeds the thickness, indicating potential transmission through the material.

Figure 9 presents ALON's ion penetration profile at different thicknesses.

Figure 9 illustrates the relationship between proton energy and penetration depth in ALON across the specified thicknesses. For the 20 µm thickness, penetration exceeds the material thickness at energies as low as 0.5 MeV, with the depth reaching up to 4000 µm at 200 MeV, indicating that most protons pass through this thin layer at higher energies, as highlighted by the shaded region. For the 100 µm thickness, penetration surpasses the threshold around 5 MeV, showing that ALON at this thickness provides limited shielding against higher-energy protons. The 2000 µm and 4000 µm thicknesses demonstrate greater stopping power, with penetration depths exceeding these thicknesses only at 50 MeV and 100 MeV, respectively. The logarithmic energy scale emphasizes the rapid increase in penetration depth at lower energies, which slows as energy increases beyond 50 MeV. These results suggest that ALON's effectiveness as a radiation shield depends heavily on its thickness and the energy of the incident protons, with thinner layers being inadequate for high-energy protons, while thicker layers provide better protection up to 100 MeV. This analysis informs the design of ALON-based shielding for applications in space or high-radiation environments, where proton energy spectra must be carefully considered.

To thoroughly assess the behavior of Aluminum Oxynitride (ALON) under proton irradiation, we analyze four essential metrics, Displacement Per Atom (DPA), Non-Ionizing Energy Loss (NIEL), ion range, and vacancies per ion, as functions of proton energy across a range of material thicknesses.

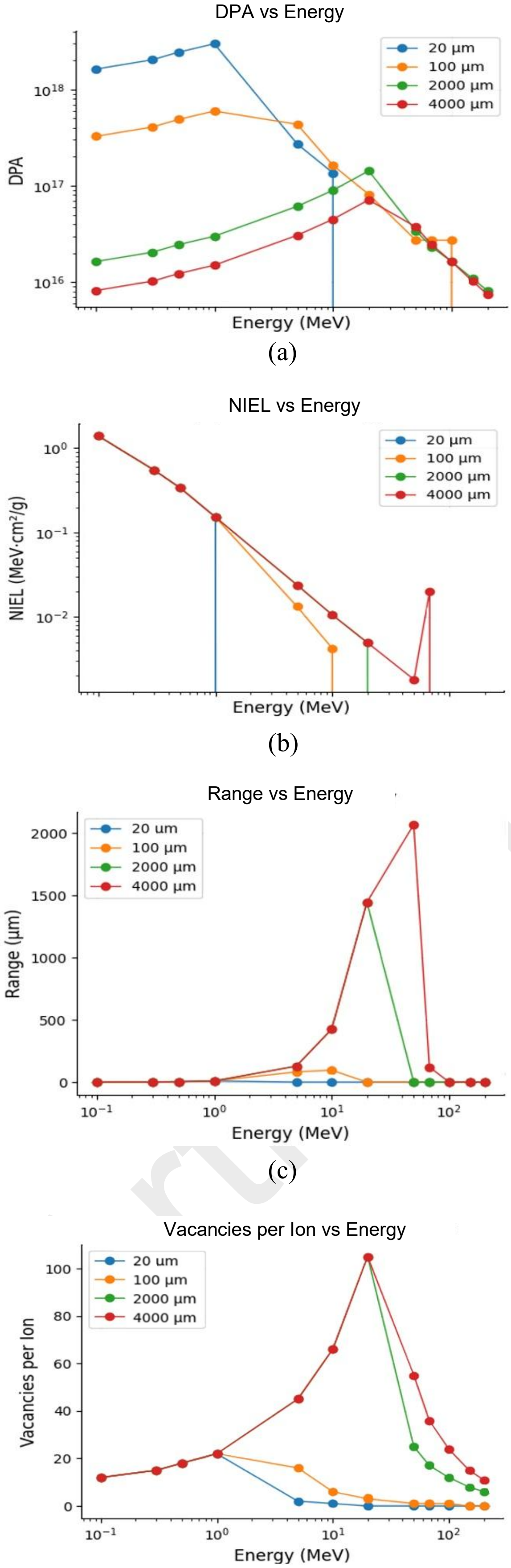

(a)

(b)

(c)

(d)

Fig. 10. Analysis of four essential metrics: (a) Displacement Per Atom (DPA), (b) Non-Ionizing Energy Loss (NIEL), (c) Ion range, and (d) Vacancies per ion.

Figure 10(a) illustrates that DPA is highest at low energies (0.1 MeV to 1 MeV), surpassing 10 DPA for all thicknesses, due to intense energy deposition near the surface, and decreases significantly for thinner layers (20 µm and 100 µm) beyond 1 MeV, dropping below 1 DPA by 10 MeV as protons pass through these layers. Thicker layers (2000 µm and 4000 µm) sustain DPA values above 0.1 up to 200 MeV, reflecting their greater ability to stop protons and accumulate damage. Hereafter, Fig. 10(b) shows a parallel trend for NIEL, peaking around 0.1 MeV·cm^2/g at low energies, with a slower decline for thicker layers due to energy deposition occurring deeper within the material. Ion range increases monotonically with energy, from nearly 0 µm at 0.1 MeV to over 4000 µm at 200 MeV, with negligible variation across thicknesses, as range is primarily determined by the material's properties and proton energy, as confirmed in Fig. 10(c). Lastly, Fig. 10(d) reveals that vacancies per ion peak around 1 MeV, reaching up to 10,000 vacancies, and decrease at higher energies as protons penetrate further with fewer interactions per unit depth, with thicker layers showing slightly higher vacancy counts due to increased stopping interactions. The logarithmic scales effectively highlight these trends across wide ranges, demonstrating that thinner ALON layers experience significant low-energy damage but are less affected at higher energies due to transmission, while thicker layers provide more consistent shielding but still face notable degradation at lower energies. These results suggest that ALON's effectiveness as a radiation shield depends on matching its thickness to the expected proton energy spectrum, with thicker layers being more suitable for broad-spectrum protection in applications such as space shielding, where both low- and high-energy protons are present.

To further assess the suitability of these materials for LEO satellite solar arrays, a Multi-Criteria Decision Analysis (MCDA) was conducted based on the simulation data and material properties. The analysis ranked materials using the following metrics: areal density (g/cm², minimized), NIEL attenuation (maximized), thermal conductivity (W/m·K, optimized), cost ($/kg, minimized), and optical clarity (maximized for ALON to ensure PV efficiency). Weights were assigned according to the LEO constellation mission profile (areal density = 0.40, NIEL = 0.30, cost = 0.20, thermal conductivity = 0.10, optical clarity = 0.10), reflecting priorities for mass constraints and radiation protection.

Table 3. MCDA results for LEO constellation mission profile.

Material	Areal Density (g/cm^2)	NIEL (MeV·cm^2/g)	Thermal Conduc. (W/m·K)	Cost ($/kg)	Score (S_j)
Aluminum	0.00081	9.93×10^{-4}	167	2.5	0.29
SiO_2	0.000696	1.2×10^{-3}	1.4	7.5	0.33
Polyimide	0.000142	1.5×10^{-3}	0.2	75	0.37
ALON	0.000368	1.0×10^{-3}	13.5	650	0.54
Ta_2O_5/Al_2O_3	0.00183	8.0×10^{-4}	27.5	1000	0.28

The composite score S_j was calculated as given in Eq. (3) for maximization metrics (NIEL attenuation, thermal conductivity, optical clarity), and $\frac{x_{i,max}-x_{ij}}{x_{i,max}-x_{i,min}}$ for minimization metrics (areal density, cost), where x_{ij} are the normalized metric values. Areal density was computed as density × thickness (e.g., 3.68 g/cm^3 × 0.0001 cm for 100 µm ALON = 0.000368 g/cm²). NIEL attenuation was inversely proportional to the peak NIEL value from Fig. 6 at 0.1 MeV (e.g., lower NIEL = higher attenuation). Thermal conductivity and cost were sourced from Table 2. Table 3 summarizes the MCDA results, showing ALON achieving the highest score (0.54), indicating its optimal balance of low areal density, good NIEL attenuation, and high optical clarity despite its higher cost. This reinforces ALON's potential as a PV shield for LEO applications.

CONCLUSION

The SRIM/TRIM simulations conducted in this study provide a comprehensive assessment of proton radiation shielding trade-offs for satellite solar arrays in LEO, with a particular focus on Aluminum Oxynitride (ALON-$Al_{23}O_{27}N_5$) as a multifunctional shielding material. Across the 0.1-200 MeV energy range, the analysis of ion penetration, vacancies per ion, projected range, Displacements Per Atom (DPA), Non-Ionizing Energy Loss (NIEL), Bragg curves, and transmission highlights the critical role of material thickness and composition in mitigating radiation damage. Baseline comparisons at 100 µm thickness reveal that high-density materials like Ta_2O_5/Al_2O_3 offer superior proton attenuation but lack optical transparency, while low-density polyimide exhibits poor shielding, underscoring the need for balanced solutions. ALON, with a density of 3.68 g/cm³, demonstrates moderate stopping power and damage resistance, with penetration depths exceeding 20 µm and 100 µm thicknesses at 0.5 MeV and 5 MeV, respectively, and 2000 µm and 4000 µm layers providing effective shielding up to 50 MeV and 100 MeV. Its high optical clarity (>80% for UV and visible light) remains intact even at 4000 µm, making it uniquely suited for protecting photovoltaic (PV) arrays without compromising energy production.

The results indicate that ALON's effectiveness as a radiation shield depends on tailoring its thickness to the proton energy spectrum. Thinner layers (20 µm and 100 µm) are vulnerable to low-energy protons (<1 MeV), where DPA and NIEL peak, but transmit high-energy protons with reduced damage. Thicker layers (2000 µm and 4000 µm) offer broader protection, sustaining higher DPA and NIEL values up to 200 MeV due to increased stopping power, though they accumulate more vacancies at intermediate energies (around 1 MeV). This trade-off, validated against literature data with 5% agreement for aluminum, suggests that ALON outperforms traditional materials like aluminum and SiO_2 in combining shielding with optical functionality, while surpassing polyimide in attenuation. The Multi-Criteria Decision Analysis (MCDA), presented in Table 3, reinforces ALON's potential, achieving the highest score (0.54) for LEO constellations where mass constraints (weight = 0.40) and radiation protection (weight = 0.30) are prioritized, outperforming aluminum (0.29), SiO_2 (0.33), polyimide (0.37), and Ta_2O_5/Al_2O_3 (0.28) due to its balanced performance and high optical clarity despite a higher cost ($500-800/kg).

These findings have significant implications for space mission design. ALON's ability to mitigate low-energy proton damage while maintaining light transmission positions it as a promising candidate for next-generation PV array shields, especially in LEO environments dominated by trapped protons and solar particle events. However, its high cost and the need for thicker layers to address high-energy protons (>100 MeV) suggest the potential for hybrid configurations with graded-Z materials or polymer-CNT composites. Future research should extend SRIM simulations with nuclear reaction codes (e.g., MCNP) to quantify secondary particle effects and validate ALON's performance under real-world spectra. This study provides a quantitative foundation for enhancing the durability and efficiency of satellite solar arrays, balancing radiation protection with mass and cost constraints in space applications.

CONFLICT OF INTEREST

The authors have no conflicts to disclose.

ACKNOWLEDGMENT

The author declares that this research received no external funding and no specific financial support from any public, commercial, or non-profit funding agencies.

AUTHOR CONTRIBUTION

C. Firat is the main and only contributor of this paper. The author read and approved the final version of the paper.

REFERENCES

1. V. U. J. Nwankwo, N. N. Jibiri and M. T. Kio, *The Impact of Space Radiation Environment on Satellites' Operation in Near-Earth Space*, in: Satellite Information Classification and Interpretation, IntechOpen, London (2020) 182.
2. J. N. Buitrago-Leiva, M. E. K. Ramouz, A. Camps *et al.*, Aero. **11** (2024) 924.
3. D. V. Reames, Space Sci. Rev. **217** (2021) 72.
4. L. Wang, Z. Zhang, X. Shen *et al.*, Front. Earth Sci. **10** (2022) 1.
5. N. N. Sulaiman, N. F. Hasbullah, N. Saidin *et al.*, Discover Mater. **5** (2025) 59.
6. C. Zeitlin, Space Radiation Shielding, in: Handbook of Bioastronautics, Springer, Cham (2020) 353.
7. H. M. Qadr, Atom Indones. **46** (2020) 47.
8. Z. Shen, X. Tang, Y. Xue, Space Solar Power Wirel. Transm. **2** (2025) 188.
9. F. Lang, M. Jošt, K. Frohna *et al.*, Joule 4 (2020) 1054.
10. A. V. Rasmetyeva, S. S. Zyryanov, I. E. Novoselov *et al.*, Nanomaterials **14** (2024) 1.
11. F. Lang, G. E. Eperon, K. Frohna *et al.*, Adv. Energy Mater. **11** (2021) 1.
12. O. Zaoui, N. Dahbi and L. Ayat, J. Ovonic Res. **16** (2020) 29.
13. L. F. Fourie, L. Square, C. Arendse *et al.*, APL Mater **11** (2023) 071103-1.
14. C. Inguimbert, IEEE Trans. Nucl. Sci. **71** (2024) 1470.
15. G. H. Kinchin and R. S. Pease, Rep. Prog. Phys. **18** (1955) 1.
16. A. Peters, M. Preindl, and V. Fthenakis, Energies **18** (2025) 509.
17. C. J. Marshall and P. W. Marshall, *Proton Effects and Test Issues for Satellite Designers, Part B: Displacement Effects*, in: NSREC Short Course, NSREC, Norfolk (1999) IV-50.
18. Z. Vahedi, A. O. Ezzati, and H. Sabri, Eur. Phys. J. Plus **139** (2024) 202.
19. L. Campajola and F. Di Capua, *Applications of Accelerators and Radiation Sources in the Field of Space Research and Industry*, in: Applications of Radiation Chemistry in the Fields of Industry, Biotechnology and Environment, Springer, Cham (2017).
20. S. Peracchi, B James, F Pagani *et al.*, IEEE Trans. Nucl. Sci. **68** (2021) 897.
21. Y. Han, T. Ying, J. Yang, *et al.*, IEEE Trans. Nucl. Sci. (2025) 1790.
22. M. Wang, Q. Wang, Y. Xiao *et al.*, Materials **18** (2025) 2558.
23. N. Baumann, K. M. Diaz, K. Simmons-Potter *et al.,* Nucl. Eng. Technol. **54** (2022) 3855.
24. A. Kannaujiya and A. P. Shah, IETE Tech. Rev. **42** (2025) 3.
25. A. J. Corso, M. Padovani, G. Santi *et al.*, ACS Appl. Mater. Interfaces **16** (2024) 38645.
26. K. Ungeheuer, J. Rybak, A. E. Bocirnea *et al.*, Appl. Sci. **15** (2025) 754.
27. Y. Han, Q. Cao, X. Chi *et al.*, IEEE Access **13** (2025) 167344.
28. D. Yun, Y. Cho, H. Shin *et al.*, Energies **18** (2025) 3378.
29. R. H. Freeman, J. Space Oper. Commun. **19** (2023) 1.
30. J. F. Ziegler, SRIM-2013. The Stopping and Range of Ions in Matter. http://www.srim.org/. Retrieved in December (2025).
31. O. Lutz, Explorer 1 Anniversary Marks 60 Years of Science in Space, https://www.jpl.nasa.gov/edu/resources/teachable-moment/explorer-1-anniversary-marks-60-years-of-science-in-space/.
Retrieved in December (2025).
32. P. J. Griffin, *Uncertainty in silicon displacement damage metrics due to the displacement threshold treatment*, in: Proceedings of the 16th European Conference on Radiation and Its Effects on Components and Systems (RADECS) (2016) 1.
33. S. Agarwal, Y. Lin, C. Li *et al.*, Nucl. Instrum. Methods Phys. Res. B **503** (2021) 11.

34. S. Chen and D. Bernard, Results Phys. **16** (2020) 102835.
35. C. Leroy and P.-G. Rancoita, Principles of Radiation Interaction in Matter and Detection, 4th ed., World Scientific Publishing, New Jersey (2016).
36. L. M. Goldman, R. Twedt, S. Balasubramanian *et al.*, *ALON Optical Ceramic Transparencies for Window, Dome, and Transparent Armor Applications*, in: Proceedings Society of Photo-Optical Instrumentation Engineers (SPIE) (2011) 801608.
37. H. Guo, S. Yang, H. Chen *et al.*, Ceram. Int. **46** (2020) 16677.
38. Y. Lin, H. Chen, J. Zhao *et al.*, Ceram. Int. **51** (2025) 5351.
39. L. Baxter, K. Herrman, R. Panthi *et al.*, *Thermoplastic micro- and nanocomposites for neutron shielding,* in: Micro and Nanostructured Composite Materials for Neutron Shielding Applications, Woodhead Publishing (2020) 53.
40. MatWeb, Polyimide, Thermoset Film, https://www.matweb.com/Search/MaterialGroupSearch.aspx?GroupID=931. Retrieved in December (2025).
41. L. An, R. Shia, X. Mao *et al.*, J. Adv. Ceram. **12** (2023) 1361.